ACS APPLIED MATERIALS & INTERFACES

www.acsami.org

Research Article

Engineering of Broadband Nanoporous Semiconductor Photonic Crystals for Visible-Light-Driven Photocatalysis

Lina Liu, Siew Yee Lim, Cheryl Suwen Law,* Bo Jin, Andrew D. Abell,* Gang Ni, and Abel Santos*

Cite This: https://dx.doi.org/10.1021/acsami.0c16914

Read Online

ACCESS | Metrics & More | Article Recommendations | Supporting Information

ABSTRACT: A new class of semiconductor photonic crystals composed of titanium dioxide (TiO_2)-functionalized nanoporous anodic alumina (NAA) broadband-distributed Bragg reflectors (BDBRs) for visible-light-driven photocatalysis is presented. NAA−BDBRs produced by double exponential pulse anodization (DEPA) show well-resolved, spectrally tunable, broad photonic stop bands (PSBs), the width of which can be precisely tuned from 70 ± 6 to 153 ± 9 nm (in air) by progressive modification of the anodization period in the input DEPA profile. Photocatalytic efficiency of TiO_2−NAA−BDBRs with tunable PSB width upon visible−NIR illumination is studied using three model photodegradation reactions of organics with absorbance bands across the visible spectral regions. Analysis of these reactions allows us to elucidate the interplay of spectral distance between red edge of TiO_2−NAA−BDBRs' PSB, electronic bandgap, and absorbance band of model organics in harnessing visible photons for photocatalysis. Photodegradation reaction efficiency is optimal when the PSB's red edge is spectrally close to the electronic bandgap of the functional semiconductor coating. Photocatalytic performance decreases dramatically when the red edge of the PSB is shifted toward visible wavelengths. However, a photocatalytic recovery is observed when the PSB's red edge is judiciously positioned within the proximity of the absorption band of model organics, indicating that TiO_2−NAA−BDBRs can harness visible electromagnetic waves to speed up photocatalytic reactions by drastically slowing the group velocity of incident photons at specific spectral regions. Our advances provide new opportunities to better understand and engineer light−matter interactions for photocatalysis, using TiO_2−NAA−BDBRs as model nanoporous semiconductor platforms. These high-performing photocatalysts could find broad applicability in visible−NIR light harvesting for environmental remediation, green energy generation, and chemical synthesis.

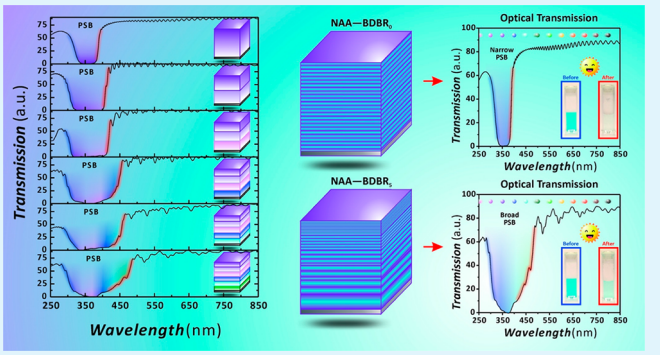

KEYWORDS: *heterogeneous photocatalysis, nanoporous anodic alumina, photonic crystals, broadband optical filters, photonic stop band, semiconductor*

1. INTRODUCTION

At the nanoscale, every photon is a precious source of energy that can be harvested for a plethora of light-based technologies such as sensing and biosensing,[1−3] optoelectronics,[4] lasing,[5] photovoltaics,[6] and photocatalysis.[7] Of all these, heterogeneous photocatalysis (i.e., "photocatalysis") is a light-driven process in which a semiconductor material converts incident photons into charge carriers (i.e., electrons and holes, e^-/h^+) to drive chemical reactions such as degradation of organics and microorganisms for air and water purification, water splitting for hydrogen (H_2) energy generation, and green synthesis and transformation of chemicals such as ammonia (NH_3) and carbon dioxide (CO_2).[8] The pioneering discovery of water splitting, the simultaneous reduction and oxidation of water, in titanium dioxide (TiO_2) electrodes by Fujishima and Honda in 1972 prompted extensive research on distinct forms of light-to-chemical energy conversion using semiconductors.[9] In this process, incident photons with energy equal to or greater than the semiconductor's electronic bandgap are absorbed by the material. Upon absorption, photons excite electrons from the valence band to the conduction band, leaving positive holes in the former band.[10] The efficiency of photocatalysis relies critically on the generation and recombination rates of excitons (i.e., e^-−h^+ pairs) upon light excitation. Exciton recombination is undesired since it transforms incident light into heat, reducing the availability of e^-−h^+ pairs that can be harvested for semiconductor-mediated redox reactions.[11] As such, efforts have focused on extending exciton lifetime via approaches such as substitutional doping,[12,13] formation of phase heterojunc-

Received: September 19, 2020
Accepted: November 30, 2020

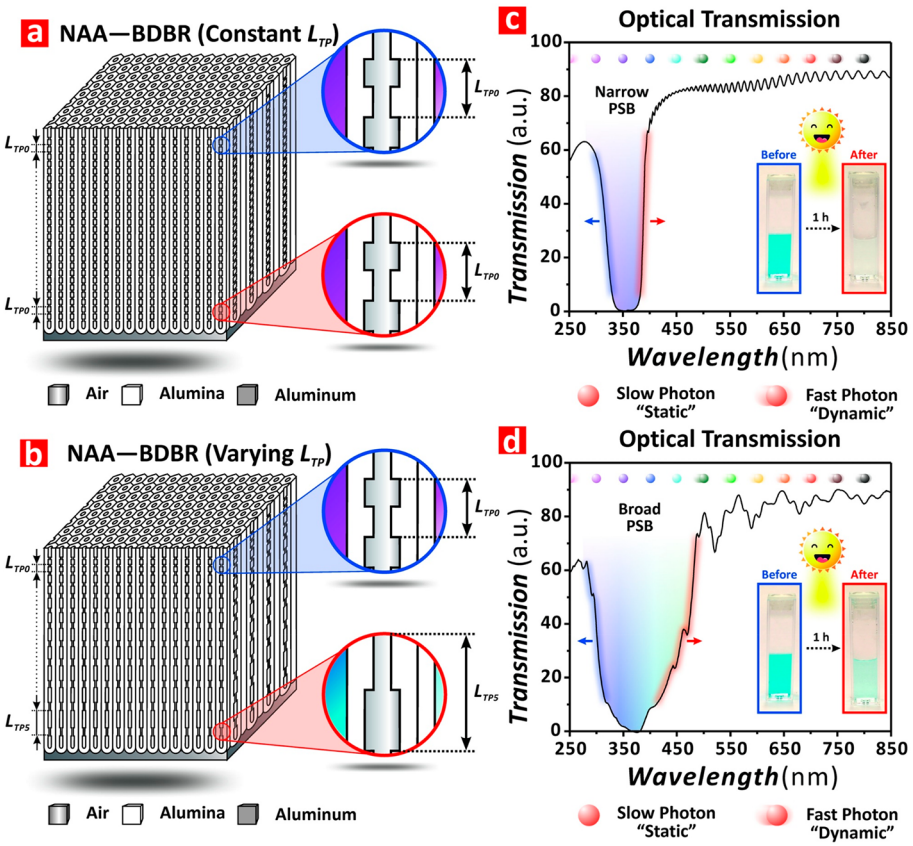

Figure 1. Fabrication and optical engineering of NAA−BDBRs by double exponential pulse anodization (DEPA). (a and b) Schematics showing the idealized structure of NAA−BDBRs fabricated with constant and varying anodization period (T_P) in the input DEPA profile, respectively, and a graphical definition of the period length, L_{TP} (i.e., distance between consecutive NAA stacks with stepwise porosity generated after each DEPA pulse). (c and d) Optical transmission spectra of representative NAA−BDBRs produced with constant and varying L_{TP}, respectively, showing details of their PSBs (in air), where blue and red arrows indicate the spectral shift of PSBs' blue and red edges upon PSB broadening by increasing L_{TP}, while the color of spheres or photons in these schematics would represent their spectral position within the UV−visible spectrum and their "static" or "dynamic" appearance would denote their slow or fast group velocity, respectively. Insets contain digital pictures showing the photodegradation (indicated by color change) of methylene blue (MB) by TiO_2−NAA−BDBRs under visible−NIR illumination conditions for 1 h of reaction. Note that (a) and (c) show a NAA−BDBR produced with a constant T_P of 600 s, while (b) and (d) show a NAA−BDBR produced with varying T_P, from T_{P0} = 600 s to T_{P5} = 755 s; fabrication conditions: double exponential current density pulses with anodization amplitude A_J = 0.420 mA cm^{-2} and current density offset J_{off} = 0.280 mA cm^{-2} in 1 M H_2SO_4 acid electrolyte at 0 °C for 750 min anodization time.

tions (e.g., anatase−rutile TiO_2),[14] hybridization of noble metal−semiconductor systems,[15,16] and nanostructural engineering of semiconductors.[17] Semiconductor thin films are inefficient for photocatalysis since electronic band bending only allows one type of charge carrier, either e^- or h^+, to be available for reaction.[18] In contrast, illumination of nanostructured semiconductors in the form of nanoparticulate aggregate films,[19] nanopillars,[20] inverted opals,[21,22] and nanoporous films[23] stimulates the generation of excitons on the semiconductor's surface. This then enables both reductive and oxidative pathways. Structural engineering of semiconductors also makes it possible to harness distinct forms of light−matter interactions such as quantum confinement,[24] slow photons,[25] surface plasmons,[26] and light recirculation.[27] These phenomena can be judiciously tailored by engineering the semiconductor's architecture, feature size, and composition to extrinsically promote exciton separation lifetimes and visible light activation toward maximizing photocatalytic performance. Nanoporous semiconductor photonic crystals (PCs) are particularly interesting platform materials for photocatalysis since they provide additional tunable features to further enhance photocatalytic efficiency including: (i) dynamic pathways for vectorial transfer of photoinduced excitons, (ii) an increased number of photoactive redox centers via a high specific surface area, and (iii) nanoporous channels to facilitate mass transport of molecules involved in redox reactions.[23] Fabrication of nanoporous semiconductor PCs by direct electrochemical oxidation (i.e., anodization) of valve metals such as titanium, vanadium, tungsten, and aluminum is a cost-competitive, time-effective, and fully scalable nanofabrication approach that enables versatile engineering of nanopore geometric features and morphology in one, two, and three dimensions.[28] Of all these, anodization of aluminum is the most mature and controllable technology to date.[29] Nanoporous anodic alumina (NAA), the anodic oxide of aluminum, was long used as a platform material to develop PC structures due to its highly tunable, self-organized, hexagonally distributed cylindrical nanopores, the nanometric features of which can be precisely engineered by the input anodization profile and conditions.[30−33] Mechanistically, NAA−PCs provide a versatile effective medium that can be tailor-engineered to control distinct forms of light−matter interactions across the broad spectrum.[34−43] Despite these advantages, NAA's intrinsic chemical structure based on

https://dx.doi.org/10.1021/acsami.0c16914
ACS Appl. Mater. Interfaces XXXX, XXX, XXX−XXX

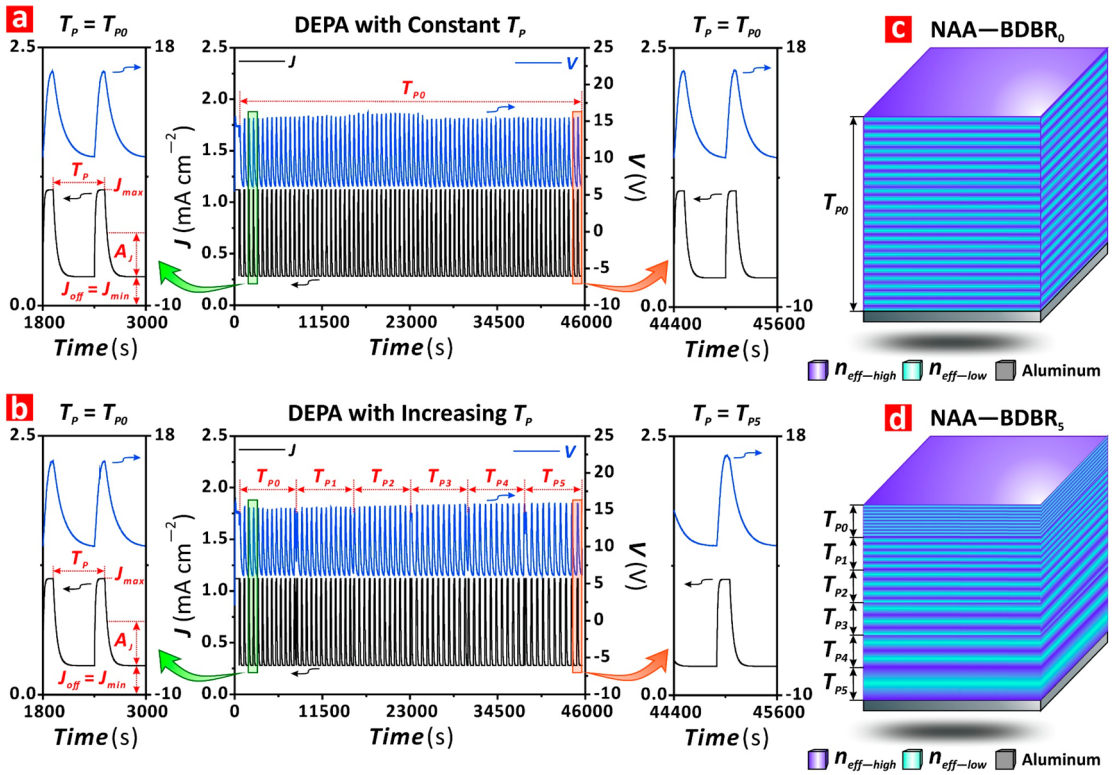

Figure 2. Structural engineering of NAA—BDBRs by double exponential pulse anodization (DEPA). (a and b) Representative full-view DEPA profiles (center) used to fabricate NAA—BDBR$_0$ with constant $T_P = T_{P0} = 600$ s, and NAA—BDBR$_5$ with increasing T_P, from $T_{P0} = 600$ to $T_{P5} = 755$ s, respectively, where green and orange rectangles correspond to magnified views of input current density pulses and output voltage response at the initial (left) and final (right) stages of the anodization process. (c and d) Schematics showing the distribution of effective refractive index between high ($n_{eff-high}$) and low ($n_{eff-low}$) values along the nanopores in NAA—BDBR$_0$ with constant T_P, and NAA—BDBR$_5$ with varying T_P in depth, respectively.

aluminum oxide (Al_2O_3) prevents it from being directly used in photocatalysis due to its electronically insulating nature (i.e., electronic bandgap ~ 9 eV). This constraint, however, can be overcome by coating NAA—PCs's surface with layers of photoactive semiconductors.[44−47] Semiconductor-functionalized NAA—PCs provide new opportunities to study fundamental aspects of light—matter interactions for photocatalysis. The structural, optical, and electronic properties of these model composite nanoporous PCs can be tailor-engineered to efficiently harvest electromagnetic waves from high-irradiance spectral regions and maximize photocatalytic reactions by rational optoelectronic designs. An outstanding example of this is the so-called "slow light" or "slow photon" effect, in which the group velocity of incident photons is substantially slowed at those spectral regions within the blue and red edges of the PC's photonic stop band (PSB).[25] Photons of these energies ("blue-edge" and "red-edge" photons) undergo multiple scattering when they propagate through the PC structure, thus enhancing optical absorption of the photoactive material by increasing the frequency of photon—atom interactions at those spectral regions where the semiconductor absorbs light inefficiently.[48]

Herein, we present a new class of nanoporous semiconductor PCs based on TiO_2-functionalized NAA broadband-distributed Bragg reflectors (TiO_2—NAA—BDBRs). NAA—BDBRs are fabricated by double exponential pulse anodization (DEPA). These NAA—PCs show well-resolved, broad PSBs, the features of which can be spectrally tuned by the input DEPA profile (Figure 1a,b). Progressive modification of the input anodization period in the input DEPA profile makes it possible to broaden the width of the PSB to judiciously position its blue and red edges at specific spectral regions (Figure 1c,d). Photocatalytic efficiency of TiO_2—NAA—BDBRs, under visible—NIR irradiation, is comprehensively studied by analyzing three model organic photodegradation reactions across the visible spectrum. We elucidate the interplay of spectral distance between blue and red edges of TiO_2—NAA—BDBRs' PSB, electronic band gap, and absorbance band of model organics in harnessing visible photons for photocatalysis.

2. EXPERIMENTAL SECTION

2.1. Materials. High-purity (99.9997%) aluminum (Al) foils with a nominal thickness of 320 μm were supplied by Goodfellow Cambridge Ltd. (UK). Hydrochloric acid (HCl), copper(II) chloride ($CuCl_2$), perchloric acid ($HClO_4$), titanium(IV) butoxide ($Ti(OBu)_4$), hydrogen peroxide (H_2O_2), methylene blue ($C_{16}H_{18}ClN_3S$, MB), rhodamine B ($C_{28}H_{31}ClN_2O_3$, RhoB), and methyl orange ($C_{14}H_{14}N_3NaO_3S$, MO) were supplied by Sigma-Aldrich (Australia) and used as received, without further purification. Ethanol (C_2H_5OH, EtOH), phosphoric acid (H_3PO_4), and sulfuric acid (H_2SO_4) were purchased from ChemSupply (Australia). All aqueous solutions used in this study were prepared with Milli—Q water (18.2 MΩ cm).

2.2. Fabrication of NAA—BDBRs by DEPA. Square Al chips with an area of 2.25 cm^2 were sequentially cleaned in ethanol and water for 15 min each under sonication at room temperature, dried, and stored until further use. Before anodization, Al chips were electropolished in a 4:1 (v/v) EtOH/$HClO_4$ electrolyte at 5 °C and 20 V for 3 min under constant stirring to achieve a nanometrically

https://dx.doi.org/10.1021/acsami.0c16914
ACS Appl. Mater. Interfaces XXXX, XXX, XXX—XXX

smooth, mirror-like surface. Electropolished Al chips were then anodized under current density control conditions in 1.5 M aqueous H_2SO_4 acid electrolyte at 0 °C. EtOH (25 vol %) was added to the acid electrolyte to prevent it from freezing at near-zero temperature.[49] Anodization was performed in electrochemical reactors equipped with a temperature-control system via custom-built cold plates connected to high-performance liquid refrigerated circulators (AC150−A25, Thermo Fisher Scientific, Australia). The acid electrolyte was stirred at a constant rate of ∼300 rpm during anodization. This process started with a 10 min step at a constant current density of 1.120 mA cm^{-2} to achieve a homogeneous nanopore growth rate. After this, anodization was automatically switched to DEPA mode for a total of 750 min, during which the current density input was pulsed between high current density (J_{max} = 1.120 mA cm^{-2}) and low current density (J_{min}= J_{off} = 0.280 mA cm^{-2}) following a double exponential pulse waveform according to eq 1:

$$J(t) = \begin{cases} J_{off} + 2{\cdot}A_J \exp\left(\frac{t}{10}\right) & \text{for } t \le (N_P T_P)/5 = \text{“raise”} \\ J_{off} + 2{\cdot}A_J{\cdot}\left[1 - \exp\left(\frac{t}{40}\right)\right] & \text{for } t > (N_P T_P)/5 = \text{“decay”} \end{cases} \quad (1)$$

where $J(t)$ is the current density at t anodization time (in seconds), A_J is the amplitude of current density (in mA cm^{-2}), J_{offset} is the current density offset (in mA cm^{-2}), N_P is an integer representing the DEPA pulse number, and T_P is the anodization period (i.e., time in seconds between DEPA pulses).

Current density−time DEPA profiles were generated by a customized LabVIEW application, using Keithley 2400C source-meters (Keithley Instruments). Figure 2a,b shows representative anodization profiles with a graphical description of the DEPA parameters used to generate these anodization profiles. After anodization, NAA−BDBRs were pore-widened by wet chemical etching in aqueous 5 wt % H_3PO_4 at 35 °C for 4 min. Six types of NAA−BDBRs were produced by systematic, progressive variation of the anodization period in the input DEPA pulses. The progressive increase of T_P at specific time points during the 750 min long anodization results in the top-down generation of stacked NAA−DBRs with increasing period length (L_{TP}) (Figure 1b). Table 1 summarizes the fabrication conditions used in our study to produce NAA−BDBRs with tunable PSB width across the UV−visible spectrum.

2.3. Surface Functionalization of NAA−BDBRs. NAA−BDBRs were chemically functionalized with semiconductor layers of TiO_2 via the sol−gel method.[44] In brief, a TiO_2 sol was prepared by mixing 97 vol % EtOH and 3 vol % $Ti(OBu)_4$ under magnetic stirring for 10 min. After mixing, NAA−BDBRs were immersed in the TiO_2 solution for 24 h, washed thoroughly with EtOH to remove TiO_2 precursor excess, and dried in an oven at 50 °C for 10 min to evaporate EtOH solvent. The resulting TiO_2−NAA−BDBRs were used to assess their photocatalytic efficiency under visible−NIR illumination conditions.

2.4. Optical Characterization of NAA−BDBRs. After fabrication, any remaining Al substrate was removed from the backside of NAA−BDBRs by chemical etching in a saturated HCl−$CuCl_2$ solution, using a 5 mm diameter circular Viton mask. Transmission spectra of NAA−BDBRs and TiO_2−NAA−BDBRs in air and water were measured at normal incidence, from 200 to 900 nm with a resolution of 1 nm, using a UV−visible spectrophotometer (Cary 300, Agilent, USA). Optical features of the characteristic PSB in the transmission spectra of NAA−BDBRs and TiO_2−NAA−BDBRs (i.e., central wavelength, λ_{PSB}; full width at half-maximum, $fwhm_{PSB}$; intensity, I_{PSB}; and blue and red edge positions, $\lambda_{PSB-blue}$ and $\lambda_{PSB-red}$) were estimated from Gaussian fittings in OriginPro 8.5, using the lower lobe of the PSB as a baseline (y_0).

Table 1. Types of NAA−BDBRs Produced in Our Study by Progressively Varying the Anodization Period (T_P) in the Input DEPA Profile

NAA−BDBR	T_P (s)	duration (min)	stacked NAA−DBRs
NAA−$BDBR_0$	T_{P0} = 600 s	750	1
NAA−$BDBR_1$	T_{P0} = 600 s	375	2
	T_{P1} = 635 s	375	
NAA−$BDBR_2$	T_{P0} = 600 s	250	3
	T_{P1} = 635 s	250	
	T_{P2} = 670 s	250	
NAA−$BDBR_3$	T_{P0} = 600 s	187.5	4
	T_{P1} = 635 s	187.5	
	T_{P2} = 670 s	187.5	
	T_{P3} = 705 s	187.5	
NAA−$BDBR_4$	T_{P0} = 600 s	150	5
	T_{P1} = 635 s	150	
	T_{P2} = 670 s	150	
	T_{P3} = 705 s	150	
	T_{P4} = 730 s	150	
NAA−$BDBR_5$	T_{P0} = 600 s	125	6
	T_{P1} = 635 s	125	
	T_{P2} = 670 s	125	
	T_{P3} = 705 s	125	
	T_{P4} = 730 s	125	
	T_{P5} = 755 s	125	

2.5. Assessment of Photocatalytic Performance of TiO_2−NAA−BDBRs under UV−Visible Illumination. The photocatalytic performance of TiO_2−NAA−BDBRs fabricated with varying T_P in the input DEPA profile (i.e., TiO_2−NAA−$BDBR_0$, TiO_2−NAA−$BDBR_1$, TiO_2−NAA−$BDBR_2$, TiO_2−NAA−$BDBR_3$, TiO_2−NAA−$BDBR_4$, and TiO_2−NAA−$BDBR_5$) was assessed under controlled visible−NIR light irradiation conditions, using photodegradation of three model organics with well-resolved absorbance bands across specific positions of the visible spectrum as model reactions: methylene blue (MB; λ_{Abs-MB} = 664 nm), rhodamine B (RhoB; $\lambda_{Abs-RhoB}$ = 554 nm), and methyl orange (MO; λ_{Abs-MO} = 464 nm) (Figure S1). Mixtures (2 mL aliquot) containing 5 mg L^{-1} model organics and 100 mM H_2O_2 were pipetted into quartz reactors. Custom-designed, 3D printed holders were used to keep TiO_2−NAA−BDBRs perpendicular to the light illumination source. TiO_2−NAA−BDBRs were immersed into the reactant solution, which was stirred for 30 min under magnetic actuation and dark conditions to achieve adsorption−desorption equilibrium before irradiation. Photocatalytic reactions were performed within dark vessels as solar simulators. Halogen lamps (HL250-A, Amscope, Australia) of 150 W (∼3000 lm) connected to the solar simulator chambers were used as simulated visible−NIR light sources. All reactions were performed at room temperature. Quantification of concentration of model organics was performed by measuring the optical absorbance of the reactant solutions at 664, 554, and 464 nm for MB, RhoB, and MO, respectively, at specific time intervals of illumination (i.e., every 15 min), using a UV−visible spectrometer (Cary 300, Agilent). Absorbance intensity was correlated with concentration of organics using calibration lines (Figure S2), and linear fittings were used to estimate the photocatalytic conversion ratio (C_t/C_o) and kinetic constant (k) according to eq 2:[50]

$$-\ln(C_t/C_o) = kt \quad (2)$$

where C_o is the concentration of organic (in mg L^{-1}) after stirring in the dark for 30 min, and C_t is the concentration of organic (in mg L^{-1}) at illumination time t (in h).

Photocatalytic degradation rates (r) were estimated as the product of the kinetic constant (k) and initial concentration of the corresponding model organic after 30 min in the dark (C_{dark}) according to eq 3:[50]

https://dx.doi.org/10.1021/acsami.0c16914
ACS Appl. Mater. Interfaces XXXX, XXX, XXX−XXX

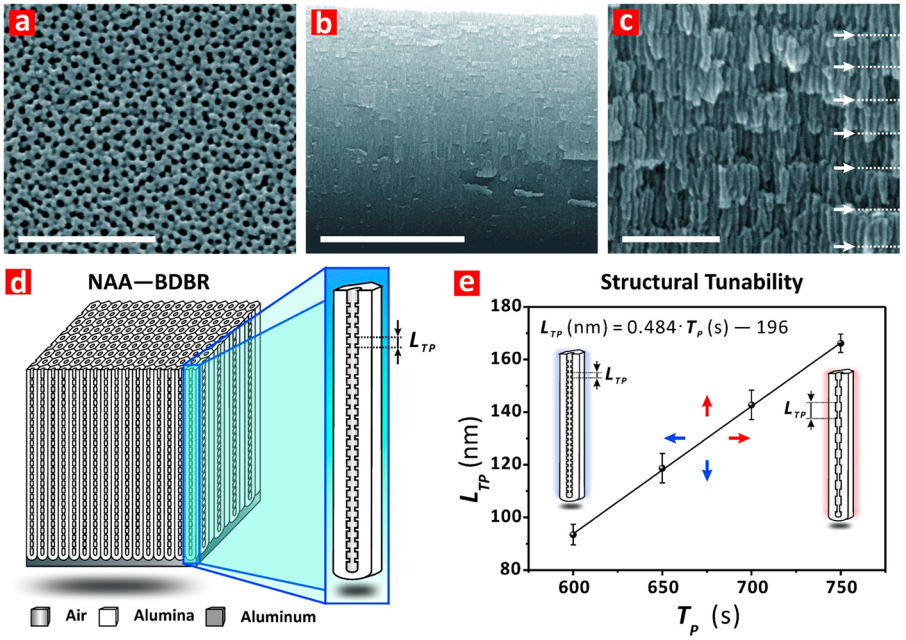

Figure 3. Structural characterization of NAA−BDBRs fabricated by DEPA. FEG-SEM images shown in (a−c) correspond to a NAA−BDBR produced in 1.5 M H_2SO_4 electrolyte at 0 °C with current density pulses of A_J = 0.420 mA cm^{-2}, J_{off} = 0.280 mA cm^{-2}, T_P = 600 s, total anodization time = 750 min, and 4 min pore widening. (a) Top view FEG-SEM image of a representative NAA−BDBR showing randomly distributed nanopores with an average size of 17 ± 2 nm (scale bar = 400 nm). (b) General cross-sectional view FEG-SEM image of a representative NAA−BDBR showing stacks of NAA with modulated porosity along their length (scale bar = 5 μm). (c) Magnified cross-sectional view FEG-SEM image of a representative NAA−BDBR showing details of nanopore modulations and period length (L_{TP}) denoted by white dotted lines and arrows (scale bar = 250 nm). (d) Schematic showing the idealized structure of NAA−BDBRs with an illustration of L_{TP} defined as the distance between adjacent NAA stacks within the NAA-based PC structure. (e) Linear fitting showing the intrinsic dependence of L_{TP} with anodization period (T_P) in the input DEPA pulses, where L_{TP} = 0.484 nm and T_P = 196 s. Blue and red arrows denote the directions of decreasing and increasing L_{TP} with T_P in the input DEPA profile, respectively.

$$r = kC_{dark} \quad (3)$$

where average values of C_{dark} for MB, RhoB, and MO after 30 min of absorption onto TiO_2−NAA−$BDBR_{0-5}$ were estimated to be 16% (0.85 ± 0.05 mg L^{-1}), 5% (0.24 ± 0.02 mg L^{-1}), and 1% (0.04 ± 0.01 mg L^{-1}) of C_o, respectively.

2.6. Chemical and Structural Characterization of NAA−BDBRs. The nanoporous structure of NAA−BDBRs produced at varying T_P was characterized by field-emission gun scanning electron microscopy (FEG-SEM Quanta 450, FEI, USA). FEG-SEM images were analyzed in ImageJ to correlate period length (L_{TP}) in NAA−BDBRs with T_P in the input DEPA profile.[51] Chemical composition of TiO_2−NAA−BDBRs was analyzed by energy dispersive X-ray (EDX) spectroscopy during FEG-SEM characterization.

RESULTS AND DISCUSSION

3.1. Structural Engineering of NAA−BDBRs by DEPA. Figure 2a,b show representative DEPA profiles used to fabricate two types of NAA−BDBRs: (i) NAA−$BDBR_0$ with constant T_P = T_{P0} = 600 s, and (ii) NAA−$BDBR_5$ with increasing T_P, from T_{P0} = 600 s to T_{P5} = 755 s. Magnified views of these anodization profiles demonstrate that asymmetric, double exponential input current density pulses result in asymmetric output voltage pulses featuring a capacitor-like charge−discharge shape (left and right insets in Figure 2a,b). This effect is attributable to the barrier oxide layer located at the nanopore bottom tips.[52] This hemispherical layer of anodic oxide, growth front of NAA at the oxide−metal interface, is composed of amorphous alumina containing aluminum (negative) and oxygen (positive) vacancies spatially distributed across its volume. Negative and positive charge vacancies slow the electric field-driven flow of electrons and ion species (i.e., Al^{3+}, O^{2-}, and OH^-) during anodization. Upon dynamic alteration of the input current density, both formation and dissolution of alumina undergo a recovery stage. During this process, both reactions change to counterbalance the electric field perturbation by adjusting the thickness of the barrier oxide layer.[53] As such, this mechano-electrochemical process leads to formation of nanopore modulations induced by the input current density pulses. The time lapse between input current density change and output voltage response (i.e, recovery time) relies on the magnitude of electric field perturbation, chemical composition and thickness of barrier oxide layer, and anodization conditions such as electrolyte temperature and its concentration. The short time delay (∼10−20 s) between input current density and output voltage pulses in these DEPA profiles is attributable to the thin barrier oxide layer (15−25 nm)[54] of NAA produced in highly concentrated sulfuric acid electrolyte, the thickness of which allows the dynamic flow of electrons and ions across it. As such, these conditions enable the precise translation of input current density pulses into nanopore modulations along the structure of NAA−BDBRs. Mechanistically, 1D NAA−BDBRs feature a spatially periodic, stepwise distribution of effective refractive index (i.e., an average of discrete refractive indexes and percentage fractions of air and alumina) that is engineered between high ($n_{eff-high}$) and low ($n_{eff-low}$) values along the nanopores by the sections of the input DEPA pulses at J_{max} and J_{min}, respectively (Figure 2c,d). This approach enables generation of a virtually infinite number of NAA−BDBRs with tunable optical properties across the broad spectrum, from UV to IR. Figure 3a−c shows a set of top and cross-

https://dx.doi.org/10.1021/acsami.0c16914
ACS Appl. Mater. Interfaces XXXX, XXX, XXX−XXX

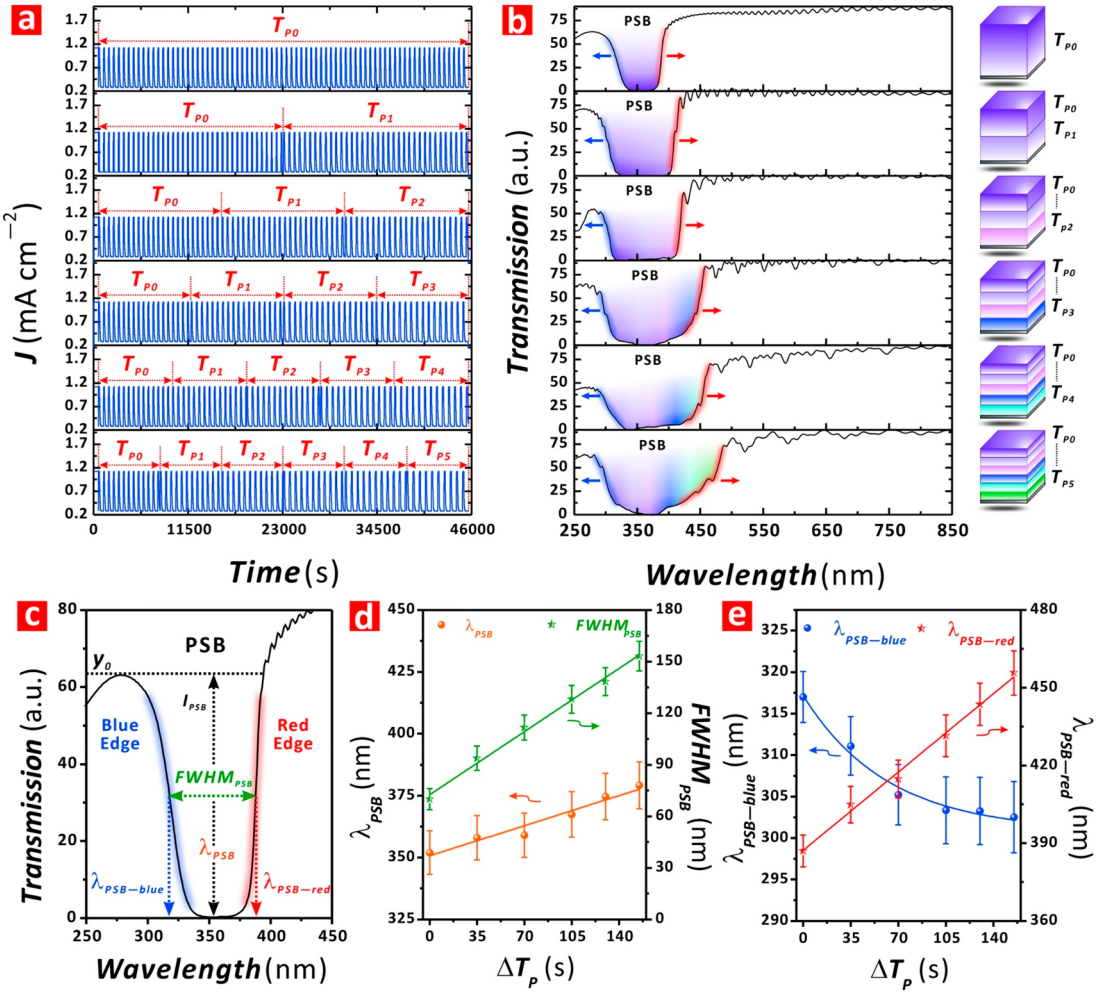

Figure 4. Engineering of NAA−BDBRs' PSB optical features by DEPA. (a) Input current density DEPA profiles used to produce NAA−BDBRs, from NAA−BDBR$_0$ (T_{P0}) to NAA−BDBR$_5$ (T_{P0}−T_{P5}). Red arrows indicate sections of the DEPA profile with fixed values of T_P as indicated in Table 1. (b) Transmission spectra of NAA−BDBRs in air, from NAA−BDBR$_0$ (T_{P0}) to NAA−BDBR$_5$ (T_{P0}−T_{P5}), showing details of their characteristic PSB, where the fill color denotes the UV−visible spectral regions in which the flow of photons is forbidden by each NAA−DBR suprastructure within the corresponding NAA−BDBR superstructure as depicted in schematics. Blue and red edges of the PSB are denoted by blue and red arrows, respectively. (c) Graphical definition of the characteristic features of the PSB of NAA−BDBRs including position of central wavelength, λ_{PSB}; full width at half-maximum, fwhm$_{PSB}$; intensity, I_{PSB}; baseline, y_0; and position of blue and red edges, $\lambda_{PSB-blue}$ and $\lambda_{PSB-red}$. Representative transmission spectrum of a NAA−BDBR$_0$ in air. (d) Linear dependence of λ_{PSB} and fwhm$_{PSB}$ with ΔT_P in the input DEPA profile, from ΔT_P = 0−155 s, in air. (e) Dependence of $\lambda_{PSB-blue}$ and $\lambda_{PSB-red}$ with ΔT_P in the input DEPA profile, from 0 to 155 s, in air.

sectional view FEG-SEM images of a representative NAA−BDBR produced with a constant T_P of 600 s. NAA−BDBRs feature characteristic arrays of nanopores randomly distributed across their top surface, of which the average diameter is measured to be 17 ± 2 nm (Figure 3a). Cross-sectional examination of these NAA-based films after mechanical fracture reveals a layered structure of one over another NAA stacks, which are induced by the current density pulses in the input DEPA profile (Figure 3b). Figure 3c shows a cross-sectional magnified view FEG-SEM image with details of NAA−BDBR nanopores featuring periodically modulated porosity along their length.

The lattice constant of these 1D NAA−PC or period length (L_{TP}) is defined as the distance between adjacent stacks of NAA within the NAA−BDBR structure (Figure 3d). This geometric parameter can be precisely engineered by the anodization period in the input DEPA pulses, where L_{TP} increases linearly with T_P at a rate of 0.484 ± 0.005 nm s^{-1} (Figure 3e).

3.2. Optical Engineering of NAA−BDBRs by DEPA.

The architecture of NAA−BDBRs can be described as a hybrid, heterogeneous PC superstructure consisting of stacked NAA−DBR suprastructures featuring constant L_{TP} (Figures 1a,b). This key geometric parameter, precisely controlled by the anodization period in the input DEPA pulses, makes it possible to judiciously engineer the features of the characteristic PSB of each NAA−DBR forming the NAA−BDBR superstructure (i.e., central wavelength position, λ_{PSB}; full width at half-maximum, fwhm$_{PSB}$; and intensity, I_{PSB}).

As such, the PSB of the NAA−BDBR superstructure results from overlapping the PSBs of NAA−DBRs embedded within its structure, each of which forbids propagation of light within specific regions. Figure 4a shows the representative DEPA profiles of the six types of NAA−BDBRs engineered in our study, the fabrication conditions of which are summarized in Table 1. Figure S3 compiles full views of these anodization profiles, which further demonstrate the precise translation of input current density DEPA pulses into asymmetric, capacitor-

https://dx.doi.org/10.1021/acsami.0c16914
ACS Appl. Mater. Interfaces XXXX, XXX, XXX−XXX

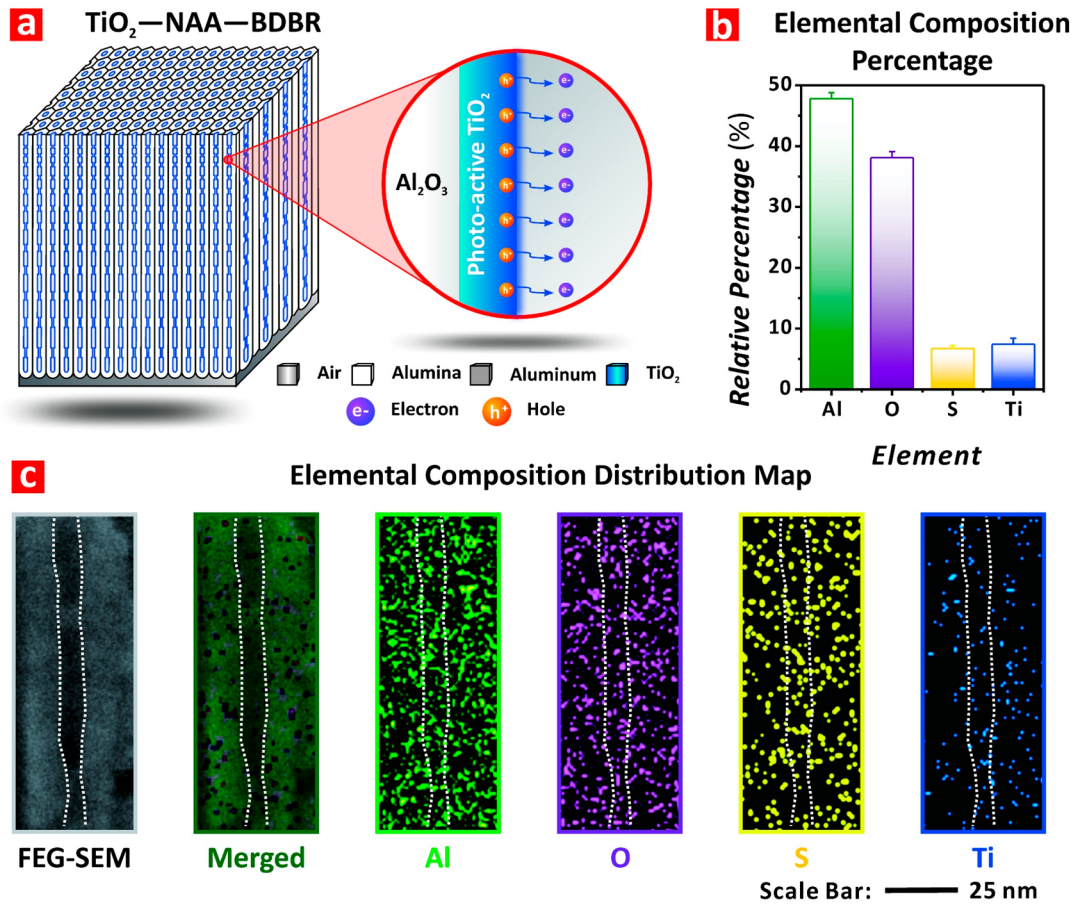

Figure 5. Chemical composition analysis of TiO_2–NAA–BDBRs fabricated by DEPA and a sol–gel method. (a) Schematic of an idealized TiO_2–NAA–BDBR illustrating its functionalized inner surface after deposition of a photoactive layer of TiO_2 via sol–gel. (b) EDX elemental composition quantification with relative percentages of Al, O, S, and Ti in a representative TiO_2–NAA–$BDBR_0$. (c) Magnified cross-sectional view FEG-SEM image and EDX elemental composition map along nanopores showing distribution of merged, Al, O, S, and Ti. White dotted lines represent nanopore boundaries from the FEG-SEM image on the left side.

like output voltage pulses. It is apparent from the transmission spectra shown in Figure 4b that NAA–BDBRs feature a characteristically intense PSB, with an average intensity of 60–80% in arbitrary transmission units. This optical feature indicates that NAA–BDBRs are highly efficient PC structures in selectively forbidding the propagation of photons within the spectral range of their PSB. It is also found that progressive increment of anodization period, from T_P = 600 to 755 s, results in a significant widening of the NAA–BDBRs' PSB. The two key spectral regions of the PSB with photocatalytic relevance are its blue and red edges (graphical description in Figure 4c), since it is in this location where the group velocity of incident photons is dramatically decreased.[55−57] This drastic reduction in group velocity is translated into an increasing frequency of light–matter interactions within the NAA–PC structure, which can be rationally harnessed to boost light-driven reactions across visible and NIR spectral regions. Figure 4d,e summarizes the dependence of characteristic features of NAA–BDBRs' PSB with increment of T_P (ΔT_P) in air, which is defined as the difference between the final and initial T_P within the DEPA profile used to produce these NAA-based PC structures. Figure 4d reveals that both λ_{PSB} and $fwhm_{PSB}$ increase linearly with ΔT_P. Linear fittings indicate that, while the former optical parameter red-shifts its position from 352 ± 9 to 379 ± 9 nm at a rate of 0.17 ± 0.02 nm s^{-1}, the latter optical feature is widened from 70 ± 6 to 153 ± 9 nm at a rate of 0.52 ± 0.02 nm s^{-1} with increasing ΔT_P. Analysis of the blue and red edges of NAA–BDBRs' PSB shown in Figure 4e indicates that the position of the PSB's blue edge ($\lambda_{PSB-blue}$) blue-shifts with ΔT_P, from 317 ± 3 to 303 ± 4 nm, following an exponential decrement trend with an apparent saturation in position shift at ~303 nm for ΔT_P > 105 s. In contrast, it is found that the position of the red edge ($\lambda_{PSB-red}$) is linearly red-shifted with increasing ΔT_P, from 387 ± 6 to 456 ± 9 nm at a rate of 0.43 ± 0.02 nm s^{-1}. These results clearly demonstrate that DEPA provides a highly controllable approach to precisely tune the PSB's features of these model PCs across the visible spectrum.

3.3. Photo-Active Functionalization of NAA–BDBRs by a Sol–Gel Method. The electronically insulating properties of NAA–BDBRs prevent the direct use of this class of nanoporous PCs as photocatalyst platforms due to the large energy band gap of Al_2O_3 (~9 eV). However, this limitation can be addressed by functionalizing the inner surface of NAA–BDBRs with layers of photoactive, semiconductor materials such as TiO_2 (Figure 5a). Six types of TiO_2–NAA–BDBRs were developed by depositing a thin TiO_2 layer within their nanopores by sol–gel method. Ellipsometry and EDX elemental map analysis of representative TiO_2 films deposited onto silicon wafers following this sol–gel protocol indicated a total thickness of 1.2 ± 0.4 nm, with good film homogeneity and distribution in composition (Figure S4).

https://dx.doi.org/10.1021/acsami.0c16914
ACS Appl. Mater. Interfaces XXXX, XXX, XXX–XXX

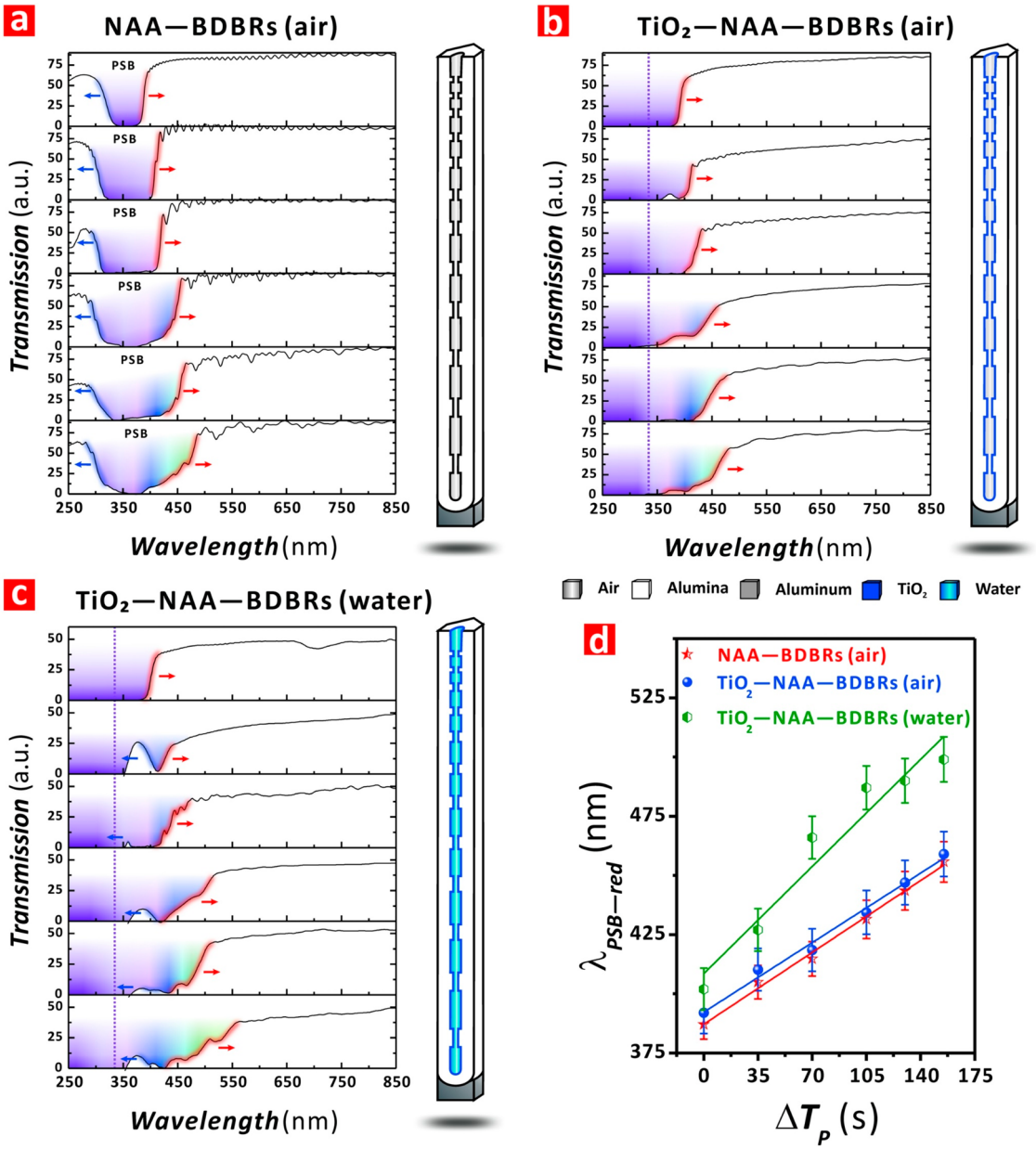

Figure 6. Analysis of spectral features of NAA−BDBRs' and TiO_2−NAA−BDBRs' PSB in air and water. Fill colors denote UV−visible spectral regions in which the flow of photons is forbidden by the PSB, and the blue and red edges of the PSB are denoted by blue and red arrows, respectively. The electronic bandgap of TiO_2 denoted by purple dashed line in (b) and (c). (a) Idealized schematic and transmission spectra of NAA−BDBRs in air, from NAA−$BDBR_0$ (T_{P0}) to NAA−$BDBR_S$ (T_{P0}−T_{PS}). (b) Idealized schematic and transmission spectra of TiO_2−NAA−BDBRs in air, from TiO_2−NAA−$BDBR_0$ (T_{P0}) to TiO_2−NAA−$BDBR_S$ (T_{P0}−T_{PS}). (c) Idealized schematic and transmission spectra of TiO_2−NAA−BDBRs in water, from TiO_2−NAA−$BDBR_0$ (T_{P0}) to TiO_2−NAA−$BDBR_S$ (T_{P0}−T_{PS}). (d) Dependence of $\lambda_{PSB-red}$ with ΔT_P in the input DEPA profile, from 0 to 155 s, for NAA−BDBRs in air (red line and dots), TiO_2−NAA−BDBRs in air (blue line and dots), and TiO_2−NAA−BDBRs in water (green line and dots).

Figure 5b summarizes the elemental composition distribution of a representative TiO_2−NAA−BDBR characterized by EDX analysis. This indicates that these composite semiconductor nanoporous structures contain 47.8 ± 0.8, 38.1 ± 0.7, 6.7 ± 0.3, and 7.4 ± 0.5% relative percentages of Al, O, S, and Ti, respectively. Al, Ti, and O atoms correspond to alumina (Al_2O_3) and titania (TiO_2), both in amorphous form, while S atoms are associated with impurities incorporated into the structure of NAA−BDBRs from the H_2SO_4 electrolyte during the DEPA process.[29] Figure 5c shows magnified cross-sectional EDX elemental map analysis of a nanopore from a representative TiO_2−NAA−BDBR indicating that Al, O, S, and Ti atoms are randomly distributed across its structure. Although the resolution of EDX is not optimal to discern the precise distribution of atoms at such low magnification, this analysis demonstrates the successful functionalization of NAA−BDBR with photoactive layers of TiO_2 via sol−gel method. Modification of the inner surface of NAA−BDBRs with functional layers of TiO_2 alters the characteristic features of their PSB. Figure 6a−c shows the optical transmission spectra of NAA−BDBRs in air, TiO_2−NAA−BDBRs in air, and TiO_2−NAA−BDBRs in water, respectively. It is apparent that the blue edge of the characteristic PSB of as-produced NAA−BDBRs vanishes upon deposition of photoactive layers

https://dx.doi.org/10.1021/acsami.0c16914
ACS Appl. Mater. Interfaces XXXX, XXX, XXX−XXX

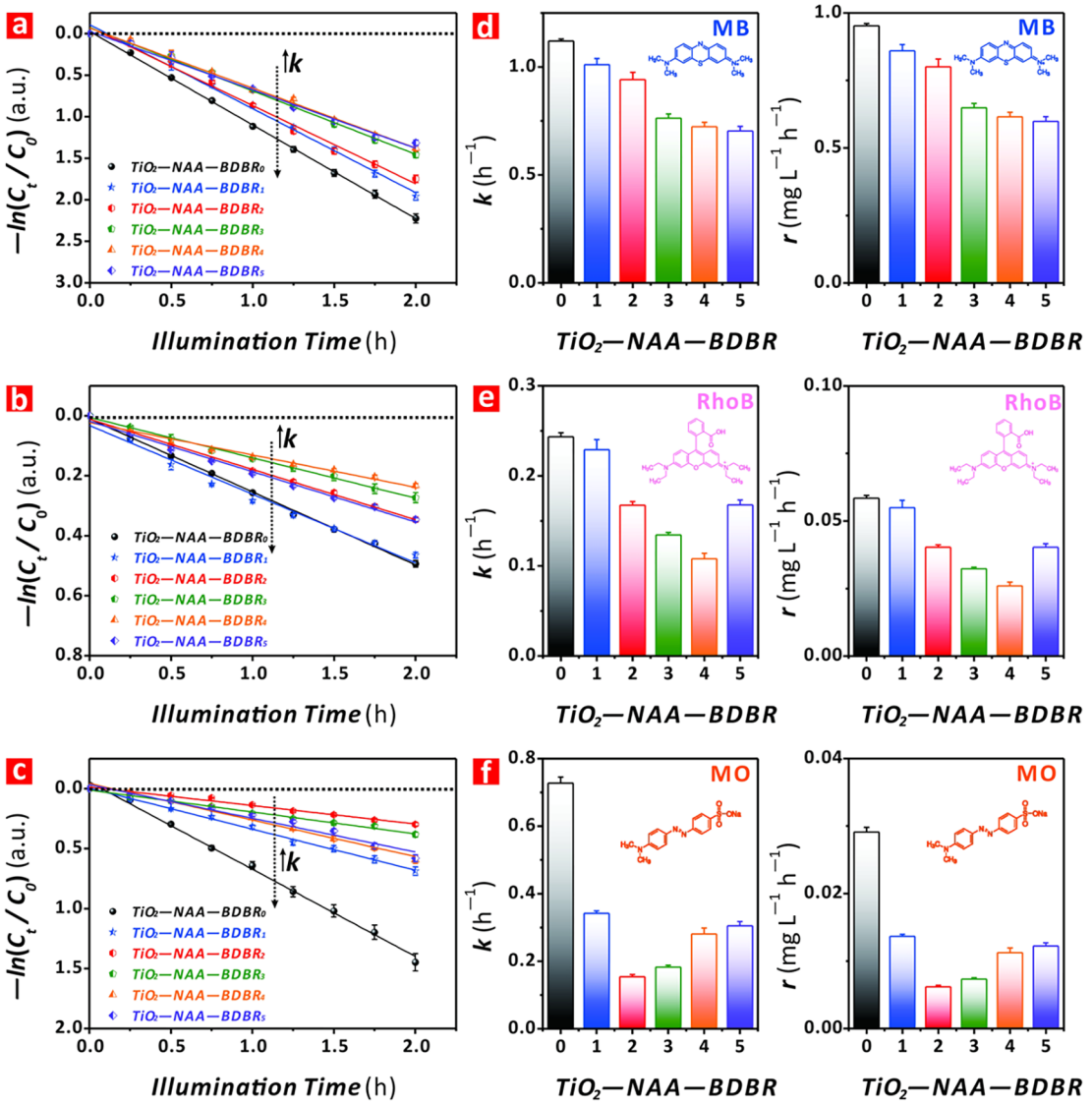

Figure 7. Photocatalytic degradation kinetics of methylene blue (MB), rhodamine B (RhoB), and methyl orange (MO) by TiO_2–NAA–BDBRs fabricated by DEPA under visible–NIR irradiation. Black dotted lines denote photodegradation of organics in control, nonfunctionalized NAA–BDBRs; error bars indicate standard deviation from three independent TiO_2–NAA–BDBRs. (a–c) Photocatalytic degradation kinetics of MB, RhoB, and MO by TiO_2–NAA–BDBRs, respectively. (d–f) Bar charts summarizing the kinetic constant (k, left) and reaction rate (r, right) for photocatalytic degradation of MB, RhoB, and MO by TiO_2–NAA–BDBRs under visible–NIR irradiation. Error bars indicate standard deviation from three independent TiO_2–NAA–BDBRs.

of TiO_2 (Figure 6b). This result is attributable to efficient optical absorption of TiO_2 at the spectral region of its electronic bandgap < ~335 nm (i.e., ~3.7 eV from diffuse reflectance estimations, Figure S5). It is also found that the average transmission intensity decreases ~10–20%, with a substantial reduction in the intensity of the characteristic interference sidelobes in the transmission spectra. The characteristic PSB of TiO_2–NAA–BDBRs undergoes spectral shifts when their effective medium is altered.[44] Photoactive layers of TiO_2 reduce the nanopore diameter in ~2 nm and also increase the local refractive index (n) within nanopores, since n_{TiO_2} = 2.61 RIU > $n_{Al_2O_3}$ = 1.77 RIU. Analysis of $\lambda_{PSB-red}$ in TiO_2–NAA–BDBRs in air reveals that $\lambda_{PSB-red}$ red-shifts 4 ± 1 nm in average its position compared to that of their as-produced NAA–BDBRs counterparts in air (Figure 6a,b). However, the linear shift rate of TiO_2–NAA–BDBRs' $\lambda_{PSB-red}$ with ΔT_P in air is found to be comparable to that of NAA–BDBRs, with a value of 0.42 ± 0.02 nm s^{-1} (Figure 6d).

Photocatalytic reactions assessed in this study are performed in aqueous-based matrices. As such, it is necessary to determine the position of $\lambda_{PSB-red}$ TiO_2–NAA–BDBRs in water. Figure 6c shows the optical transmission spectra of TiO_2–NAA–BDBR$_{0-5}$ in water, where it is apparent that $\lambda_{PSB-red}$ undergoes a significant redshift when the refractive index of the medium filling the nanopores is increased from n_{air} = 1.00 RIU to n_{water} = 1.33 RIU. Qualitative analysis of these spectra also reveals a significant reduction in transmission intensity, which can be attributed to light absorption by water molecules filling the nanopores. Interestingly, the PSB's blue edge of TiO_2–NAA–BDBR$_{1-5}$ raises again when the position of the PSB is red-shifted far enough from the optical absorption range of the TiO_2 functional layer (i.e., > 335 nm). Analysis of $\lambda_{PSB-red}$ of TiO_2–NAA–BDBRs' PSB shown

https://dx.doi.org/10.1021/acsami.0c16914
ACS Appl. Mater. Interfaces XXXX, XXX, XXX–XXX

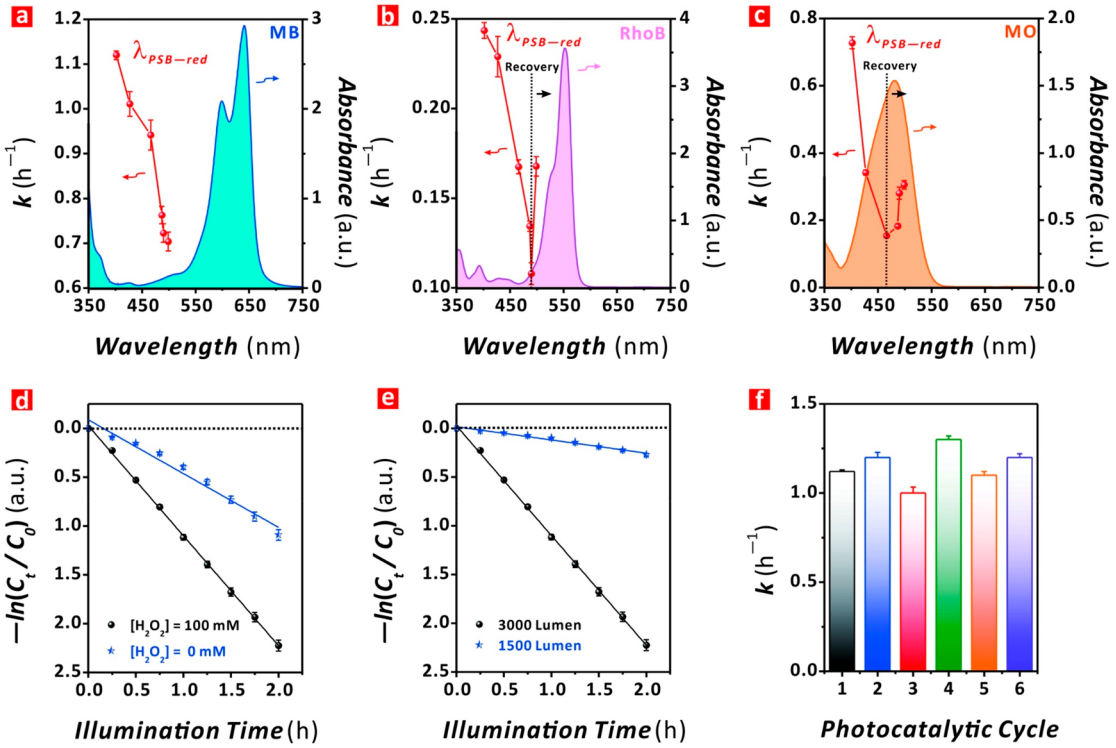

Figure 8. Spectral arrangement of red edge of PSB in TiO_2−NAA−BDBRs in water ($\lambda_{PSB-red}$) and absorbance spectrum of (a) MB, (b) RhoB, and (c) MO, and kinetic constant (k) values for these model reactions. Black dotted lines in (b) and (c) denote spectral regions with photocatalytic enhancements associated with slow photons. Control experiments demonstrating the effect of (d) H_2O_2 for [H_2O_2] = 0 and 100 mM, (e) illumination intensity at 1500 and 3000 lm, and reusability for six photocatalytic cycles. Reactions performed using MB as model organic and a TiO_2−NAA−$BDBR_0$.

in Figure 6c indicates that the position of the PSB's red edge is linearly red-shifted with increasing ΔT_p, from 402 ± 9 to 499 ± 9 nm at a rate of 0.65 ± 0.08 nm s^{-1} (Figure 6d).

3.4. Photocatalytic Performance of TiO_2−NAA−BDBRs under Visible−NIR Illumination. The photocatalytic performance of six types of TiO_2−NAA−BDBRs (i.e., TiO_2−NAA−$BDBR_{0-5}$) with precisely engineered PSBs across the UV−visible spectrum was comprehensively investigated using three model photodegradation reactions at specific visible spectral regions under visible−NIR illumination conditions. Absorbance intensity of MB, RhoB, and MO reactant solutions at 664, 554, and 464 nm, respectively, was used to determine the photocatalytic kinetic constant (k) and reaction rates (r) (i.e., performance indicators) of these model reactions driven by visible−NIR light in the presence of TiO_2−NAA−BDBRs. The spectral distribution of simulated visible−NIR light in our study was approximately 0.1% UV (350−400 nm), 64.9% visible (400−750 nm), and 35.0% NIR (800−1025 nm) (Figure S6). Therefore, these photocatalytic reactions were performed under illumination conditions that were spectrally distant from the experimentally determined energy bandgap of TiO_2 (i.e., 3.7 eV = 335 nm). Figure 7a−c shows the linearized pseudo-first-order photodegradation kinetic of MB, RhoB, and MO under the conditions of study for TiO_2−NAA−$BDBR_{0-5}$. The kinetic constant and the reaction rate of these reactions for each type of TiO_2−NAA−BDBR, which correspond to the slope of linear fittings shown in Figure 7a−c and Table S1 and their product with C_{dark} are summarized in Figure 7d−f in the form of bar charts.

Analysis of k values for photodegradation of MB by TiO_2−NAA−BDBRs indicates a 37.5% decrease in photocatalytic performance with increasing $fwhm_{PSB}$, from an initial value of 1.12 ± 0.01 h^{-1} to a final of 0.70 ± 0.02 h^{-1} for TiO_2−NAA−$BDBR_0$ and TiO_2−NAA−$BDBR_5$, respectively (Figure 7d). This trend is also observed for RhoB, although a sharp recovery in photocatalytic performance is found for TiO_2−NAA−$BDBR_5$. Values of k for this system decrease dramatically from 0.24 ± 0.01 to 0.11 ± 0.01 h^{-1} for TiO_2−NAA−$BDBR_0$ and TiO_2−NAA−$BDBR_4$, respectively, and increase to 0.17 ± 0.02 h^{-1} for TiO_2−NAA−$BDBR_5$ (Figure 7e). Figure 7f shows the photodegradation of MO by TiO_2−NAA−BDBRs as a function of $fwhm_{PSB}$. It is apparent from these results that photocatalytic performance initially decreases with increasing $fwhm_{PSB}$, where k is reduced from 0.72 ± 0.02 to 0.15 ± 0.01 h^{-1} for TiO_2−NAA−$BDBR_0$ and TiO_2−NAA−$BDBR_2$, respectively. After reaching its minimum, k increases with $fwhm_{PSB}$, from 0.15 ± 0.01 h^{-1} for TiO_2−NAA−$BDBR_0$ to 0.31 ± 0.01 h^{-1} for TiO_2−NAA−$BDBR_5$. These trends are also observed for the rates of these reactions, where the maximum and minimum values of r were measured to be r_{max} = 0.95 ± 0.01, 0.06 ± 0.01, and 0.03 ± 0.01 mg L^{-1} h^{-1} and r_{min} = 0.60 ± 0.02, 0.03 ± 0.01, and 0.006 ± 0.002 mg L^{-1} h^{-1} for MB, RhoB, and MO, respectively.

3.5. Understanding the Slow Photon Effect in TiO_2−NAA−BDBRs. The characteristic PSB of TiO_2−NAA−BDBRs is the spectral region or range of wavelengths where the flow of incident photons is forbidden by the PC's structure. As such, incoming photons of these specific energies or wavelengths cannot be harnessed to drive photocatalytic reactions due to efficient scattering and reflection by the semiconductor PC. However, photons within the vicinity of the blue and red edges of the PCs' PSB (i.e., left and right regions of the band, where

https://dx.doi.org/10.1021/acsami.0c16914
ACS Appl. Mater. Interfaces XXXX, XXX, XXX−XXX

Table 2. Photocatalytic Kinetic Constants (k) Comparison for the Photo-Degradation of MB, RhoB, and MO by Various Benchmark TiO_2-Based Photocatalyst Materials under Visible−NIR Illumination Conditions

photocatalyst	optical mechanism	model organic			ref
		MB	RhoB	MO	
P25 TiO_2 nanoparticles		0.64 h^{-1}	0.17 h^{-1}	0.00 h^{-1}	58
TiO_2 inverse opal	slow photon	1.32 h^{-1}	0.47 h^{-1}	0.01 h^{-1}	58
TiO_2−NAA−GIFs	slow photon	2.10 h^{-1}	0.39 h^{-1}	0.25 h^{-1}	44
TiO_2−NAA−DBRs	slow photon	3.04 h^{-1}	0.35 h^{-1}	0.32 h^{-1}	45
TiO_2−NAA−μQVs	light recirculation	3.55 h^{-1}	1.34 h^{-1}	0.77 h^{-1}	27
TiO_2−NAA−BDBRs	slow photon	1.12 h^{-1}	0.24 h^{-1}	0.73 h^{-1}	this study

it becomes almost flat) propagate through the PC structure with strongly reduced group velocity. This phenomenon, the so-called "slow photons", increases the frequency of light−matter interactions within the PC structure. These interactions can be rationally managed to boost the generation of e^-−h^+ pairs by the TiO_2 photoactive layer. Localization of slow photons occurs in the high (i.e., photocatalysts) and low (i.e., reactant solution) dielectric sections of the red and blue edge of the PC's PSB, respectively. Since $\lambda_{PSB-blue}$ of TiO_2−NAA−BDBRs is mostly located within the electronic bandgap of the TiO_2 coating (i.e., the absorption region of the semiconductor), it is possible to assume that the contribution of slow photons to photocatalytic enhancements is exclusively associated with $\lambda_{PSB-red}$. Analysis of the relative spectral arrangement of TiO_2−NAA−BDBRs' $\lambda_{PSB-red}$ in water, TiO_2 electronic bandgap, and absorbance spectra of MB, RhoB, and MO, and the corresponding values of kinetic constant as a photocatalytic performance indicator was carried out to elucidate the mechanistic contribution of slow photons in driving photocatalytic reactions by TiO_2−NAA−BDBRs. Figure 8a displays values of k with the spectral arrangement of $\lambda_{PSB-red}$ in TiO_2−NAA−$BDBR_{0-5}$, the electronic bandgap of TiO_2, and the absorbance spectrum of MB. It is apparent from that graph that under such a configuration, where the absorbance band of MB is positioned far away (∼165−262 nm) from the red edge of TiO_2−NAA−$BDBR_{0-5}$'s PSB, photocatalytic kinetic performance decays dramatically (∼37.5%) when $\lambda_{PSB-red}$ is red-shifted upon widening of PSB by increasing T_P in the input DEPA profile. Analysis of RhoB photodegradation by TiO_2−NAA−$BDBR_{0-5}$ shown in Figure 8b reveals an initially sharp decrease in photocatalytic performance, in which k is reduced ∼46% from TiO_2−NAA−$BDBR_0$ to TiO_2−NAA−$BDBR_4$. The red edge of TiO_2−NAA−$BDBR_{0-4}$ is located at ∼55−152 nm far from the absorbance band maximum of RhoB. However, when $\lambda_{PSB-red}$ is close to the blue edge of the absorbance band of RhoB for TiO_2−NAA−$BDBR_5$, k undergoes a recovery of ∼65%, characterized by a sharp rise. The absorbance band of MO is the closest to the red edge of TiO_2−NAA−BDBRs, with its maximum centered at 464 nm. It is apparent from Figure 8c that the photocatalytic recovery stage in this system is much more sustained than that of RhoB, due to the overlapping between $\lambda_{PSB-red}$ and absorbance band of MO. Although photocatalytic performance decreases ∼80% from TiO_2−NAA−$BDBR_0$ to TiO_2−NAA−$BDBR_2$, k recovers progressively to ∼50% of its original value when $\lambda_{PSB-red}$ is red-shifted from 466 ± 1 nm (TiO_2−NAA−$BDBR_2$) to 499 ± 1 nm (TiO_2−NAA−$BDBR_5$), respectively.

3.6. Photocatalytic Degradation Mechanism in TiO_2−NAA−BDBRs. We propose a double mechanism to describe the photocatalytic degradation of organics by TiO_2−NAA−BDBRs under 400−1025 nm irradiation. Upon light irradiation, photoactivation of the functional TiO_2 layer deposited onto the inner surface of TiO_2−NAA−BDBRs generates e^-−h^+ pairs in its conduction and valence bands, respectively. Photoexcited h^+ drive the oxidation of H_2O molecules in the aqueous reactant solution in contact with the photoactive TiO_2 layer. This reaction leads to the generation of OH· radicals, which subsequently transform organic molecules into CO_2 and H_2O. Simultaneously, the reaction of H_2O_2 molecules with photoexcited e^- results in OH· radicals and OH^- ions which are further oxidized into OH· radicals by photoexcited h^+ in the valence band of the photoactive TiO_2 layer. Figure 8d shows the photocatalytic degradation of MB by a TiO_2−NAA−$BDBR_0$ with and without addition of H_2O_2 to the reactant solution (i.e., for $[H_2O_2]$ = 100 and 0 mM, respectively). This control experiment demonstrates that MB can be partially degraded without the presence of H_2O_2 in the reactant solution, where k is measured to be 1.12 ± 0.01 and 0.55 ± 0.03 h^{-1}. Therefore, this mechanism alone cannot account for the total photocatalytic efficiency of TiO_2−NAA−BDBRs. Li et al. demonstrated that when dye-sensitized semiconductor photonic crystals are illuminated by visible light the dye molecules are excited to singlet and triplet states through intersystem crossing.[56] This process is followed by electron injection into the conduction band of the photoactive TiO_2 layer. The injected electrons reduce the number of chemisorbed oxidant molecules (i.e., O_2) onto the semiconductor layer to yield oxidizing species such as superoxide radical anions O_2^- and subsequently ·OH radicals, which are the main cause of organics photodegradation. The efficiency of this process is maximum when the red edge of the characteristic PSB of model PCs is spectrally aligned with the absorbance maximum of dyes across the visible spectrum. In fact, analysis of the spectral arrangement of PSB's red edge, the electronic bandgap of functional semiconductor, and the absorbance band of model organic indicates that photocatalytic efficiency is optimal when the PSB is closely aligned with the electronic bandgap of TiO_2. However, approximately 50−65% recovery in performance of visible−NIR-light-driven reaction rates can be judiciously engineered by positioning the PSB's red edge within the absorbance band of model organics. These photocatalytic enhancements are attributable to slow photons at those spectral regions where the PSB of TiO_2−NAA−BDBRs dramatically reduces the group velocity of irradiated photons. As a result, the lifespan of visible photons is extended within the semiconductor, increasing the frequency of light−matter interactions that result in extra e^-−h^+ pairs that can subsequently be more efficiently harvested to accelerate photocatalytic reactions at spectral regions that are far from the semiconductor's electronic bandgap. Photocatalytic reactions in TiO_2−NAA−BDBRs also rely strongly on the

https://dx.doi.org/10.1021/acsami.0c16914
ACS Appl. Mater. Interfaces XXXX, XXX, XXX−XXX

intensity of illumination. Figure 8e shows photodegradation kinetics of MB by a TiO_2−NAA−$BDBR_0$ at a visible−NIR illumination of 1500 and 3000 lm. It is apparent that this parameter has a dramatic effect on the photocatalytic efficiency of these model semiconductor PCs, where k decreases from 1.12 ± 0.01 to 0.14 ± 0.01 h^{-1} at 3000 and 1500 lm, respectively (i.e., ∼78% decrement in performance). Reusability is a critical aspect that any photocatalyst platform material must fulfill to satisfy the requirements of real-world applications. Photocatalysts that can be used for several cycles can significantly reduce running costs by increasing the lifespan and long-term use of the material, minimizing translational cost, and favoring technological adaptation by industry. Figure 8f summarizes the photocatalytic kinetics performance of a model TiO_2−NAA−$BDBR_0$ in degrading MB for six cycles of 2 h each under visible−NIR illumination. It is found that k values fluctuate from a maximum of 1.30 ± 0.03 h^{-1} to a minimum of 1.00 ± 0.02 h^{-1}, with an average value of 1.15 ± 0.01 h^{-1}. The residual deviation of this process is found to be ∼9%, which clearly demonstrates the capability of TiO_2−NAA−BDBR over extended photocatalytic uses to satisfy the requirements of industrial applications.

3.7. Benchmarking of TiO_2−NAA−BDBRs. Table 2 shows a performance comparison of benchmark photocatalyst platforms in degrading MB, RhoB, and MO under visible light illumination conditions, using distinct forms of nanoporous photonic crystals. At first glance, it is clear that TiO_2−NAA−BDBRs provide better photocatalytic performance than that of P25 TiO_2 nanoparticles, a benchmark photocatalyst, for all organics analyzed in this study.[58] It is also apparent from this comparison that TiO_2−NAA−BDBRs achieve a performance comparable to that of TiO_2-based inverted opal structures developed by Zheng et al. in the photodegradation of MB.[58] However, other NAA-based PCs such as gradient-index filters (TiO_2−NAA−GIFs),[44] distributed Bragg reflectors (TiO_2−NAA−DBRs),[45] and optical microcavities (TiO_2−NAA−μQVs)[27] provide much higher performances that that of TiO_2−NAA−BDBRs. We hypothesize that this result is attributable to the wide, intense characteristic PSB of TiO_2−NAA−BDBRs, which results in a much more efficient reflection of incoming light across a broader range of wavelengths and in turn minimizes their overall photocatalytic performance. Interestingly, TiO_2−NAA−BDBRs achieve a performance comparable to that of other NAA−PCs in the photodegradation of RhoB molecules and performance superior to that of inverted opals, TiO_2−NAA−GIFs, and TiO_2−NAA−DBRs to degrade MO molecules under visible−NIR illumination conditions. This result could be associated with a more efficient utilization of slow photons by this new form of NAA−PC at those spectral regions where alignment with the optical absorbance maxima of the model organic is optimal.

CONCLUSIONS

In summary, TiO_2−NAA−BDBRs provide an ideal photocatalyst platform to better understand and control slow photons for visible−NIR light-driven photocatalysis. The optoelectronic properties of this new class of semiconductor PCs can be precisely engineered by combining double exponential pulse anodization with deposition of functional photoactive layers of semiconductors. This fully scalable technique provides simplicity, controllability, and versatility in tailoring the features of the characteristic PSB of NAA−BDBRs and the electronic bandgap of the functional semiconductor. NAA−BDBRs with well-resolved, spectrally tunable, broad PSBs of varying width, from 70 ± 6 to 153 ± 9 nm, can be produced by judicious modification of the anodization profile in the input DEPA profile. Modification of the inner surface of these nanoporous PCs with thin, functional, photoactive layers of TiO_2 provides a means of harnessing incident visible−NIR photons to efficiently generate charge carriers to drive photocatalytic reactions. Comprehensive analysis of the relative spectral arrangement of TiO_2−NAA−BDBRs' PSB red edge, the TiO_2 electronic band gap, and the absorbance band of model organics allows us to elucidate the mechanism of slow photons in these semiconductor PCs. Our findings reveal that photocatalytic efficiency is maximum when the PSB's red edge is aligned with the electronic bandgap of the semiconductor. However, a recovery of ∼65% in the reaction rate performance under visible−NIR light illumination can be engineered by deliberately positioning the PSB's red edge within the absorbance band of model organics. Photocatalytic enhancements associated with slow photons are attributable to extended lifespan of visible photons, sensitization of the semiconductor in close proximity to organic molecules, and the concomitant increase in the frequency of photon−atom interactions at spectral regions far from TiO_2 electronic bandgap.

Our results provide exciting new opportunities to engineer light−matter interactions for photocatalysis, using TiO_2−NAA−BDBRs as model photocatalyst platforms. These findings could find broad applicability across light-harvesting disciplines such as chemical synthesis, environmental remediation, and green energy generation.

ASSOCIATED CONTENT

Supporting Information

The Supporting Information is available free of charge at https://pubs.acs.org/doi/10.1021/acsami.0c16914.

Further information on calibration lines correlating organic molecules concentration and absorbance intensity, absorbance spectra of organic molecules, estimations of homogeneity and electronic bandgap of TiO_2 thin films deposited by the sol−gel method, the spectrum of simulated solar light irradiation used in our study, summary of photocatalytic performances, and full-view anodization profiles used to engineer the optical properties of TiO_2−NAA−BDBRs across the visible spectrum (PDF)

AUTHOR INFORMATION

Corresponding Authors

Andrew D. Abell − *Institute for Photonics and Advanced Sensing, ARC Centre of Excellence for Nanoscale BioPhotonics, and Department of Chemistry, The University of Adelaide, Adelaide, South Australia 5005, Australia;* orcid.org/0000-0002-0604-2629; Email: andrew.abell@adelaide.edu.au

Cheryl Suwen Law − *School of Chemical Engineering and Advanced Materials, Institute for Photonics and Advanced Sensing, and ARC Centre of Excellence for Nanoscale BioPhotonics, The University of Adelaide, Adelaide, South Australia 5005, Australia*; Email: suwen.law@adelaide.edu.au

https://dx.doi.org/10.1021/acsami.0c16914
ACS Appl. Mater. Interfaces XXXX, XXX, XXX−XXX

Abel Santos − *School of Chemical Engineering and Advanced Materials, Institute for Photonics and Advanced Sensing, and ARC Centre of Excellence for Nanoscale BioPhotonics, The University of Adelaide, Adelaide, South Australia 5005, Australia;* orcid.org/0000-0002-5081-5684; Email: abel.santos@adelaide.edu.au

Authors

Lina Liu − *School of Chemical Engineering and Advanced Materials, The University of Adelaide, Adelaide, South Australia 5005, Australia; State Key Laboratory of High-efficiency Utilization of Coal and Green Chemical Engineering and College of Chemistry and Chemical Engineering, Ningxia University, Yinchuan 750021, PR China*

Siew Yee Lim − *School of Chemical Engineering and Advanced Materials, Institute for Photonics and Advanced Sensing, and ARC Centre of Excellence for Nanoscale BioPhotonics, The University of Adelaide, Adelaide, South Australia 5005, Australia*

Bo Jin − *School of Chemical Engineering and Advanced Materials, The University of Adelaide, Adelaide, South Australia 5005, Australia;* orcid.org/0000-0003-4491-8465

Gang Ni − *State Key Laboratory of High-efficiency Utilization of Coal and Green Chemical Engineering and College of Chemistry and Chemical Engineering, Ningxia University, Yinchuan 750021, PR China*

Complete contact information is available at: https://pubs.acs.org/10.1021/acsami.0c16914

Notes

The authors declare no competing financial interest.

■ ACKNOWLEDGMENTS

The authors acknowledge and pay their respects to the Kaurna−Adelaide people, the Traditional Custodians of the land on which the work was performed. The authors also acknowledge the support provided by the Australian Research Council through the grants CE140100003 and DP200102614, the School of Chemical Engineering and Advanced Materials, The University of Adelaide, the Institute for Photonics and Advanced Sensing (IPAS), the ARC Centre of Excellence for Nanoscale BioPhotonics (CNBP), the National Natural Science Foundation of China through grant numbers 21567021, 21765016, and 21765017, and the National First-Rate Discipline Construction Project of Ningxia (Chemical Engineering and Technology, NXYLXK2017A04).

■ REFERENCES

(1) Huang, S.; Romero-Ruiz, M.; Castell, O. K.; Bayley, H.; Wallace, M. I. High-Throughput Optical Sensing of Nucleic Acids in a Nanopore Array. *Nat. Nanotechnol.* **2015**, *10*, 986−991.

(2) Fan, X.; White, I. M. Optofluidic Microsystems for Chemical and Biological Analysis. *Nat. Photonics* **2011**, *5*, 591−597.

(3) Li, M.; Ling, J.; He, Y.; Javid, U. A.; Xue, S.; Lin, Q. Lithium Niobate Photonic-Crystal Electro-Optic Modulator. *Nat. Commun.* **2020**, *11*, 4123.

(4) Qin, C.; Sandanayaka, A. S. D.; Zhao, C.; Matsushima, T.; Zhang, D.; Fujihara, T.; Adachi, C. Stable Room-Temperature Continuous-Wave Lasing in Quasi-2D Perovskite Films. *Nature* **2020**, *585*, 53−57.

(5) Tandaechanurat, A.; Ishida, S.; Guimard, D.; Nomura, M.; Iwamoto, S.; Arakawa, Y. Lasing Oscillation in a Three-Dimensional Photonic Crystal Nanocavity with a Complete Bandgap. *Nat. Photonics* **2011**, *5*, 91−94.

(6) Brongersma, M. L.; Cui, Y.; Fan, S. Light Management for Photovoltaics using High-Index Nanostructures. *Nat. Mater.* **2014**, *13*, 451−460.

(7) Sato, S.; Morikawa, T.; Saeki, S.; Kajino, T.; Motohiro, T. Visible-Light-Induced Selective CO_2 Reduction Utilizing a Ruthenium Complex Electrocatalyst Linked to a p-Type Nitrogen-Doped Ta_2O_5 Semiconductor. *Angew. Chem., Int. Ed.* **2010**, *49*, 5101−5105.

(8) Fox, M. A.; Dulay, M. T. Heterogeneous Photocatalysis. *Chem. Rev.* **1993**, *93*, 341−357.

(9) Fujishima, A.; Honda, K. Electrochemical Photolysis of Water at a Semiconductor Electrode. *Nature* **1972**, *238*, 37−38.

(10) Osterloh, F. E. Inorganic Nanostructures for Photoelectrochemical and Photocatalytic Water Splitting. *Chem. Soc. Rev.* **2013**, *42*, 2294−2320.

(11) Gao, M.; Liu, H.; Yu, S.; Louisia, S.; Zhang, Y.; Nenon, D. P.; Alivisatos, A. P.; Yang, P. Scaling Laws of Exciton Recombination Kinetics in Low Dimensional Halide Perovskite Nanostructures. *J. Am. Chem. Soc.* **2020**, *142*, 8871−8879.

(12) Liu, G.; Wang, L.; Yang, H. G.; Cheng, H.-M.; Lu, G. Q. Titania-Based Photocatalysts-Crystal Growth, Doping and Heterostructuring. *J. Mater. Chem.* **2010**, *20*, 831−843.

(13) Kisch, H. Semiconductor Photocatalysis−Mechanistic and Synthetic Aspects. *Angew. Chem., Int. Ed.* **2013**, *52*, 812−847.

(14) Low, J.; Yu, J.; Jaroniec, M.; Wageh, S.; Al-Ghamdi, A. A. Heterojunction Photocatalysis. *Adv. Mater.* **2017**, *29*, 1601694.

(15) Wang, M.; Ye, M.; Iocozzia, J.; Lin, C.; Lin, Z. Plasmon-Mediated Solar Energy Conversion via Photocatalysis in Noble Metal/Semiconductor Composites. *Adv. Sci.* **2016**, *3*, 1600024.

(16) Serpone, N.; Emeline, A. V. Semiconductor Photocatalysis − Past, Present, and Future Outlook. *J. Phys. Chem. Lett.* **2012**, *3*, 673−677.

(17) Jung, H. S.; Hong, Y. J.; Li, Y.; Cho, J.; Kim, Y. − J.; Yi, G. − C. Photocatalysis Using GaN Nanowires. *ACS Nano* **2008**, *2*, 637−642.

(18) Gudat, W.; Eastman, D. E. Electronic Surface Properties of III-V Semiconductors: Excitonic Effects, Band-Bending Effects, and Interactions with Au and O Adsorbate Layers. *J. Vac. Sci. Technol.* **1976**, *13*, 831−837.

(19) Song, X. − M.; Wu, J. − M.; Yan, M. Photocatalytic Degradation of Selected Dyes by Titania Thin Films with Various Nanostructures. *Thin Solid Films* **2009**, *517*, 4341−4347.

(20) Shao, M.; Cheng, L.; Zhang, X.; Ma, D. D. D.; Lee, S. − T. Excellent Photocatalysis of HF-Treated Silicon Nanowires. *J. Am. Chem. Soc.* **2009**, *131*, 17738−17739.

(21) Sordello, F.; Duca, C.; Maurino, V.; Minero, C. Photocatalytic Metamaterials: TiO_2 Inverse Opals. *Chem. Commun.* **2011**, *47*, 6147−6149.

(22) Chen, J. I. L.; von Freymann, G.; Kitaev, V.; Ozin, G. A. Effect of Disorder on the Optically Amplified Photocatalytic Efficiency of Titania Inverse Opals. *J. Am. Chem. Soc.* **2007**, *129*, 1196−1202.

(23) Lim, S. Y.; Law, C. S.; Liu, L.; Markovic, M.; Hedrich, C.; Blick, R. H.; Abell, A. D.; Zierold, R.; Santos, A. Electrochemical Engineering of Nanoporous Materials for Photocatalysis: Fundamentals, Advances, and Perspectives. *Catalysts* **2019**, *9*, 988.

(24) Edvinsson, T. Optical Quantum Confinement and Photocatalytic Properties in Two-, One- and Zero-Dimensional Nanostructures. *R. Soc. Open Sci.* **2018**, *5*, 180387.

(25) Liu, J.; Zhao, H.; Wu, M.; Van der Schueren, B.; Li, Y.; Deparis, O.; Ye, J.; Ozin, G. A.; Hasan, T.; Su, B.-L. Slow Photons for Photocatalysis and Photovoltaics. *Adv. Mater.* **2017**, *29*, 1605349.

(26) Lim, S. Y.; Law, C. S.; Bertó-Roselló, F.; Liu, L.; Markovic, M.; Ferré-Borrull, J.; Abell, A. D.; Voelcker, N. H.; Marsal, L. F.; Santos, A. Tailor-Engineered Plasmonic Single-Lattices: Harnessing Localized Surface Plasmon Resonances for Visible-NIR Light-Enhanced Photocatalysis. *Catal. Sci. Technol.* **2020**, *10*, 3195−3211.

(27) Liu, L.; Lim, S. Y.; Law, C. S.; Jin, B.; Abell, A. D.; Ni, G.; Santos, A. Light-Confining Semiconductor Nanoporous Anodic

Alumina Optical Microcavities for Photocatalysis. *J. Mater. Chem. A* **2019**, *7*, 22514−22529.
(28) Ghicov, A.; Schmuki, P. Self-Ordering Electrochemistry: A Review on Growth and Functionality of TiO_2 Nanotubes and Other Self-Aligned MO_x Structures. *Chem. Commun.* **2009**, *20*, 2791−2808.
(29) Lee, W.; Park, S. − J. Porous Anodic Aluminum Oxide: Anodization and Templated Synthesis of Functional Nanostructures. *Chem. Rev.* **2014**, *114*, 7487−7556.
(30) Masuda, H.; Ohya, M.; Asoh, H.; Nakao, M.; Nohtomi, M.; Tamamura, T. Photonic Crystal Using Anodic Porous Alumina. *Jpn. J. Appl. Phys.* **1999**, *38*, L1403−L1405.
(31) Masuda, H.; Ohya, M.; Nishio, K.; Asoh, H.; Nakao, M.; Nohtomi, M.; Yokoo, A.; Tamamura, T. Photonic Band Gap in Anodic Porous Alumina with Extremely High Aspect Ratio Formed in Phosphoric Acid Solution. *Jpn. J. Appl. Phys.* **2000**, *39*, L1039−L1041.
(32) Masuda, H.; Ohya, M.; Asoh, H.; Nishio, K. Photonic Band Gap in Naturally Ocurring Ordered Anodic Porous Alumina. *Jpn. J. Appl. Phys.* **2001**, *40*, L1217−L1219.
(33) Santos, A. Nanoporous Anodic Alumina Photonic Crystals: Fundamentals, Developments and Perspectives. *J. Mater. Chem. C* **2017**, *5*, 5581−5599.
(34) Yisen, L.; Yi, C.; Zhiyuan, L.; Xing, H.; Yi, L. Structural Coloring of Aluminum. *Electrochem. Commun.* **2011**, *13*, 1336−1339.
(35) Rahman, M. M.; Marsal, L. F.; Pallarès, J.; Ferré-Borrull, J. Tuning the Photonic Stop Bands of Nanoporous Anodic Alumina-Based Distributed Bragg Reflectors by Pore Widening. *ACS Appl. Mater. Interfaces* **2013**, *5*, 13375−13381.
(36) Macias, G.; Ferré-Borrull, J.; Pallarès, J.; Marsal, L. F. 1-D Nanoporous Anodic Alumina Rugate Filters by Means of Small Current Variations for Real-Time Sensing Applications. *Nanoscale Res. Lett.* **2014**, *9*, 315.
(37) Santos, A.; Yoo, J. H.; Rohatgi, C. V.; Kumeria, T.; Wang, Y.; Losic, D. Realisation and Advanced Engineering of True Optical Rugate Filters Based on Nanoporous Anodic Alumina by Sinusoidal Pulse Anodisation. *Nanoscale* **2016**, *8*, 1360−1373.
(38) Santos, A.; Pereira, T.; Law, C. S.; Losic, D. Rational Engineering of Nanoporous Anodic Alumina Optical Bandpass Filters. *Nanoscale* **2016**, *8*, 14846−14857.
(39) Kushnir, S. E.; Pchelyakova, T. Y.; Napolskii, K. S. Anodizing with Voltage *versus* Optical Path Length Modulation: A New Tool for the Preparation of Photonic Structures. *J. Mater. Chem. C* **2018**, *6*, 12192−12199.
(40) Santos, A.; Law, C. S.; Pereira, T.; Losic, D. Nanoporous Hard Data: Optical Encoding of Information within Nanoporous Anodic Alumina Photonic Crystals. *Nanoscale* **2016**, *8*, 8091−8100.
(41) Law, C. S.; Lim, S. Y.; Macalincag, R. M.; Abell, A. D.; Santos, A. Light-Confining Nanoporous Anodic Alumina Microcavities by Apodized Stepwise Pulse Anodization. *ACS Appl. Nano Mater.* **2018**, *1*, 4418−4434.
(42) Law, C. S.; Lim, S. Y.; Abell, A. D.; Marsal, L. M.; Santos, A. Structural Tailoring of Nanoporous Anodic Alumina Optical Microcavities for Enhanced Resonant Recirculation of Light. *Nanoscale* **2018**, *10*, 14139−14152.
(43) Lee, J.; Bae, K.; Kang, G.; Choi, M.; Baek, S.; Yoo, D. − S.; Lee, C. − W.; Kim, K. Graded-Lattice AAO Photonic Crystal Heterostructure for High *Q* Refractive Index Sensing. *RSC Adv.* **2015**, *5*, 71770−71777.
(44) Lim, S. Y.; Law, C. S.; Markovic, M.; Kirby, J. K.; Abell, A. D.; Santos, A. Engineering the Slow Photon Effect in Photoactive Nanoporous Anodic Alumina Gradient-Index Filters for Photocatalysis. *ACS Appl. Mater. Interfaces* **2018**, *10*, 24124−24136.
(45) Lim, S. Y.; Law, C. S.; Markovic, M.; Marsal, L. F.; Voelcker, N. H.; Abell, A. D.; Santos, A. Rational Management of Photons for Enhanced Photocatalysis in Structurally-Colored Nanoporous Anodic Alumina Photonic Crystals. *ACS Appl. Energy Mater.* **2019**, *2*, 1169−1184.
(46) Cuevas, A. L.; Martínez de Yuso, M.; Vega, V.; González, A. S.; Prida, V. M.; Benavente, J. Influence of ALD Coating Layers on the Optical Properties of Nanoporous Alumina-Based Structures. *Coatings* **2019**, *9*, 43.
(47) Bachmann, J.; Zierold, R.; Chong, Y. T.; Hauert, R.; Sturm, C.; Schmidt-Grund, R.; Rheinländer, B.; Grundmann, M.; Gösele, U.; Nielsch, K. A Practical, Self-Catalytic, Atomic Layer Deposition of Silicon Dioxide. *Angew. Chem., Int. Ed.* **2008**, *47*, 6177−6179.
(48) Likodimos, V. Photonic Crystal-Assisted Visible Light Activated TiO_2 Photocatalysis. *Appl. Catal., B* **2018**, *230*, 269−303.
(49) Wang, Y.; Santos, A.; Evdokiou, A.; Losic, D. Rational Design of Ultra-Short Anodic Alumina Nanotubes by Short-Time Pulse Anodization. *Electrochim. Acta* **2015**, *154*, 379−386.
(50) Diamantopoulou, A.; Sakellis, E.; Gardelis, S.; Tsoutsou, D.; Glenis, S.; Boukos, N.; Dimoulas, A.; Likodimos, V. Advanced Photocatalysts Based on Reduced Nanographene Oxide-TiO_2 Photonic Crystal Films. *Materials* **2019**, *12*, 2518.
(51) Abràmoff, M. D.; Magalhaes, P. J.; Ram, S. J. Image Processing with ImageJ. *Biophotonics Int.* **2004**, *11*, 36−42.
(52) Lee, W.; Kim, J. C. Highly Ordered Porous Alumina with Tailor-Made Pore Structures Fabricated by Pulse Anodization. *Nanotechnology* **2010**, *21*, 485304.
(53) Lee, W.; Kim, J. − C.; Gösele, U. Spontaneous Current Oscillations during Hard Anodization of Aluminum under Potentiostatic Conditions. *Adv. Funct. Mater.* **2010**, *20*, 21−27.
(54) Chen, Y.; Santos, A.; Ho, D.; Wang, Y.; Kumeria, T.; Li, J.; Wang, C.; Losic, D. On The Generation of Interferometric Colors in High Purity and Technical Grade Aluminum: An Alternative Green Process for Metal Finishing Industry. *Electrochim. Acta* **2015**, *174*, 672−681.
(55) Baba, T. Slow Light in Photonic Crystals. *Nat. Photonics* **2008**, *2*, 465−473.
(56) Noda, S.; Chutinan, A.; Imada, M. Trapping and Emission of Photons by a Single Defect in a Photonic Bandgap Structure. *Nature* **2000**, *407*, 608−610.
(57) Li, Y.; Kunitake, T.; Fujikawa, S. Efficient Fabrication and Enhanced Photocatalytic Activities of 3D-Ordered Films of Titania Hollow Spheres. *J. Phys. Chem. B* **2006**, *110*, 13000−13004.
(58) Zheng, X.; Meng, J.; Chen, J.; Wang, J.; Xian, J.; Shao, Y.; Fu, X.; Li, D. *J. Phys. Chem. C* **2013**, *117*, 21263−21273.

https://dx.doi.org/10.1021/acsami.0c16914
ACS Appl. Mater. Interfaces XXXX, XXX, XXX−XXX